Supplementary Materials for

Structural basis of nucleosome-dependent cGAS inhibition

Joshua A. Boyer[#], Cathy J. Spangler[#], Joshua D. Strauss[#], Andrew P. Cesmat, Pengda Liu, Robert K. McGinty*, Qi Zhang*

#These authors contributed equally to this work.
*Correspondence to rmcginty@email.unc.edu (R.K.M.); zhangqi@unc.edu (Q.Z.)

This PDF file includes:

Other Supplementary Materials for this manuscript include the following:

Materials and Methods

Protein expression and purification

A modified pET-28(a) vector with an N-terminal His_6-SUMO tagged-mcGAS catalytic domain (residues 141-507) was transformed into *E. coli* BL21(DE3) and expressed at 15°C following induction with IPTG, as described previously (*17*). The recombinant cGAS catalytic domain was purified with nickel affinity chromatography and the SUMO fusion-tag was removed via SUMO protease. Following a second nickel column, the protein was further purified using size-exclusion chromatography, eluting in 20 mM Tris pH 7.5, 150 mM NaCl, and 5 mM DTT. Histone H2A, H2B, H3, and H4 were cloned into pST50Tr vectors. Tailless ($H2A_{13-119}$, $H2B_{37-125}$, $H3_{34-135}$, and $H4_{20-102}$), acidic patch mutant (H2A: E61A, E64S, N68A, D72S, N89A, D90A, E91S), and point mutant histones were mutated in these backgrounds (*34*). Recombinant histones were expressed, purified, and reconstituted with 147 bp of the 601 DNA sequence into human nucleosome core particles (NCP) with the nucleosome-positioning sequence centered in the DNA fragment, as previously described (*33*). The cGAS-NCP complex was formed by combining the cGAS catalytic domain and NCP at final concentrations of 75 μM and 25 μM, respectively. The mixture was set on ice for 45 mins and the excess cGAS was removed via a Superdex 200 increase 10/300GL gel filtration column equilibrated in 20 mM HEPES pH 7.5, 150 mM NaCl, 1 mM TCEP. Immediately following elution, complex-containing fractions were concentrated to 1 mg/mL, transferred on ice, and blotted on grids.

Cryo-EM data collection

Cryo-EM grids were prepared with a Vitrobot Mark IV (Thermo Fisher Scientific) set to room temperature and 95% humidity. Quantifoil R1.2/1.3 copper 400 mesh grids were rendered hydrophilic by glow-discharging for 30 seconds at 15 mA with a Pelco easiGlow. 4 μl of sample were applied directly to the carbon side of the TEM grid then blotted with Whatman 595 filter paper for 3 seconds with the blot force set to -10. Cryo-EM grids were imaged with a Thermo Fisher Scientific 200 kV TEM Talos Arctica G3 equipped with a Gatan K3 direct electron detector. The microscope was aligned, and beam was set parallel at spot size 3 with the 70 μm condenser and 100 μm objective apertures (*35, 36*). Data was collected with SerialEM using a multi-shot record of a 3 X 3 regular pattern (*37*). One movie was collected over each hole and 9 movies were collected for each stage shift. Movies (dose rate 15 e-/pixel/second, 60 frames, and a total dose 53 e-/Å2) were collected in counting mode at 57,500 x nominal magnification, corresponding to a

pixel size of 0.91 Å, with a defocus range of -0.6 to -3.1 µm. A total of 2,100 movies were saved as unprocessed Tiff (LZW compressed) files for analysis.

Image processing and 3D reconstruction

The movies were imported into RELION-3.1-beta (*38*) in optics groupings based on beam-image shifts used during data collection. Whole-frame motion correction was carried out with the RELION implementation of MotionCor2, followed by CTF estimation with CTFFIND4.1 (*39*). All micrographs with CTF-estimated maximum resolution above 5 Å were omitted from the analysis, leaving 1,937 micrographs. Particles were initially picked using the RELION Laplacian-of-Gaussian (LoG) method. These particles were used to generate 2D references for a subsequent round of template-based autopicking in RELION. After iterative rounds of 2D classification, a set of 433,445 particles were subjected to a 3D classification into four classes. One of the resulting classes (Class 1; 92,555 particles) from this initial 3D classification showed a 1:1 complex of cGAS bound to the nucleosome, whereas another class (Class 4; 116,866 particles) showed a 2:1 complex.

Particles from the 1:1 cGAS-NCP complex class were refined with no symmetry (C1) to an initial resolution of 4.35 Å. After Bayesian particle polishing and higher order aberration correction (CTF refinement) in RELION, the resolution improved to 3.66 Å. Particles initially classified into the 2:1 cGAS-NCP complex class that were later reclassified as 1:1 were then added to the 1:1 complex particle set. Another round of 3D classification was conducted along with two rounds of CTF refinement, yielding a 3.41 Å reconstruction of the 1:1 cGAS-NCP complex from 70,790 particles. Particles initially classified as a 2:1 cGAS-NCP complex were also refined to an initial resolution of 4.35 Å. Bayesian particle polishing and CTF refinement improved the resolution to 3.49 Å. A subsequent 3D classification resulted in a more convincingly 2:1 bound particle subset (45,587 particles) that could be successfully refined with C2 symmetry. Two additional rounds of CTF refinement of these particles resulted in a 3.30 Å reconstruction of the 2:1 cGAS-NCP complex.

To maximize overall resolution at a single cGAS-NCP interface, the particles from the 1:1 and 2:1 cGAS-NCP reconstructions were combined (116,377 particles) and refined to 3.26 Å resolution. High resolution features in this map are visible throughout the nucleosome and into the nucleosome-interacting face of cGAS. However, more distal regions of cGAS are less well

resolved. Multibody refinement with masks around cGAS and the nucleosome shows clear cGAS motion along the principal components of the analysis, with the first three eigenvectors accounting for 49% of the variance in the data. Although the nucleosome density remains highly resolved through multibody refinement, cGAS resolution is limited to secondary structural elements. The limiting resolution in the distal region of cGAS is likely due the structural heterogeneity indicated by multibody refinement, and was difficult to improve with masking or signal subtraction methods due to the small size of cGAS (~40kDa). Instead, we carried out an additional round of 3D classification using local angular searches (± 5°) to isolate a particle set with a more homogeneous cGAS conformation. This classification identified several 1:1 cGAS-NCP classes with distinct cGAS conformations (Classes 3, 4 and 6). Masked refinement of the most populated of these classes (Class 6; 44,311 particles) resulted in a 3.9 Å reconstruction with greatly improved global cGAS density. After model-building, the 3.26 Å 1:1 cGAS-NCP map and the 3.9 Å $cGAS_{mask}$-NCP map were combined using Phenix combine_focused_maps, resulting in a composite map displaying the best-fitting parts of each map to the model. 3DFSC (*40*) and RELION-3.1-beta (*38*) were used to examine directional resolution and local resolution, respectively.

Model building and refinement

The 3.26 Å map of the 1:1 cGAS-NCP complex was sharpened in Phenix (version 1.18) (*41*) and models of the nucleosome (PDBID: 6FQ5) (*22*) and mouse cGAS (PBDID: 4K8V chain C) (*15*) were docked into the sharpened map using Phenix dock_in_map. Through docking of several available nucleosome models, we found that the selected nucleosome EM model provided the best starting model for refinement and fit our map better than comparable crystal structures. Chain C of the tetrameric mouse cGAS was selected due its low crystallographic B-factor and similar backbone conformation relative to other chains in the asymmetric unit of 4K8V. Amino acids in the *X. laevis* histones present in the initial model were substituted with the human sequences and changes to the DNA sequence in the terminal 3 bp of the 601 sequence relative to the model were made in Coot. The sequence-corrected model was refined using iterative rounds of real space refinement in Phenix and manual model building in Coot. To minimize over-refinement, additional iterative rounds of real space refinement and manual building were performed against one of the masked, sharpened half-maps ($Half_{work}$). The resulting final model showed strong correlation to both the full map and the other half-map ($Half_{test}$) as well as the 3.9 Å $cGAS_{mask}$-NCP

reconstruction. Reference model restraints were applied (sigma = 1) using chain C of 4K8V for all residues with per residue map to model correlations less than 0.65. This limited improper modeling into noisier regions of the map. The 3.30 Å C2 map was used to solve the 2:1 cGAS-NCP complex similarly, starting with the initial real space refined model generated for the 1:1 complex. Only one copy of cGAS was modeled into the 2:1 map. Models and map-model correlations were validated using MolProbity (*42*) and EMRinger (*43*) in Phenix (version 1.18) (*41*).

cGAS activity assay

20 µL *in vitro* reactions were assembled in PCR tubes with final concentrations of 0.5 µM purified cGAS protein, 5 µM dsDNA (45 bp), and varying wild-type, histone tailless, and acidic-patch mutant nucleosome core particle concentrations in reaction buffer (22 mM HEPES pH 7.5, 5.5 mM $MgCl_2$, 5 mM DTT, 3 µM $ZnCl_2$, 1.25 U of Inorganic Pyrophosphatase (Sigma) (final concentrations)). Reactions were initiated with the addition of 2 mM (each) GTP/ATP mix containing ~12.5 nM ^{32}P-α-ATP (Perkin-Elmer) and incubated at 37°C for 15 min. Reactions were quenched with equal volumes of gel loading buffer (95% formamide, 10 mM EDTA, xylene cyanol and bromophenol blue loading dyes) and ran on a TBE/7M Urea/15% polyacrylamide gel. Gels were exposed to a phosphoimager plate, scanned with an Amersham Typhoon 5 Biomolecular imager (GE Healthcare) and quantified using peak volume and rubberbanding for background subtraction in Image Quant software (GE Healthcare). All assays were carried out in triplicate to estimate experimental errors. Student's t-tests were used to compare experimental means. Triplicate assays were performed at least two times.

Electrophoretic mobility-shift assays

Electrophoretic mobility shift assays (EMSA) were performed by combining 25 nM wild-type or mutant NCP with varying concentrations of purified cGAS protein in binding buffer (20 mM Tris-Cl, pH 7.6, 50 mM NaCl, 0.25 mM EDTA, 1 mM TCEP, 5% sucrose) in a final volume of 50 µl. Mixtures were incubated at room temperature for 30 min. Samples were analyzed on 10% polyacrylamide gels run in 0.2x TBE at 150 V for 60–90 min at 4°C. Native gels were stained with ethidium bromide and visualized using a ChemiDoc MP Imaging System (Bio-Rad). EMSA analysis was performed at least two times.

Size-exclusion chromatography-multi-angle light scattering (SEC-MALS)

SEC-MALS was performed for determining molar mass of the cGAS-NCP complex and free NCP. The complex sample was prepared at ~1.25 mg/ml with a 3:1 molar ratio for cGAS:NCP and the free NCP sample was prepared at ~0.75 mg/ml in a buffer of 20 mM Tris pH 7.5, 150 mM NaCl, and 5 mM DTT. 200 µl of the samples were applied to a Superdex 200 HR 10/300 GL gel filtration column (GE Healthcare) in the same buffer at a flow rate of 0.3 ml/min at room temperature, followed by passing through a HELEOS II in-line enhanced optimal system laser photometer (Wyatt Technology) coupled to a T-rEX inferometric refractometer (Wyatt Technology) for measuring light scattering for MW and refractive index changes for concentration, respectively. Data analysis was performed using Astra software version 6.3 (Wyatt Technology) with a dn/dc value of 0.175 ml/g as described previously (*44*).

Size-exclusion chromatography binding assays

Size-exclusion chromatography was used to analyze cGAS binding to wild-type and mutant NCP. cGAS and NCP were mixed at 3 and 1 µM concentrations, respectively, in a buffer of 20 mM Tris pH 7.5, 150 mM NaCl, and 5 mM DTT and analyzed on a Superdex 200 increase 10/300GL gel filtration column pre-equilibrated in the same buffer. Baseline correction was applied using default values in Unicorn 5.11 Evaluation software (GE Healthcare).

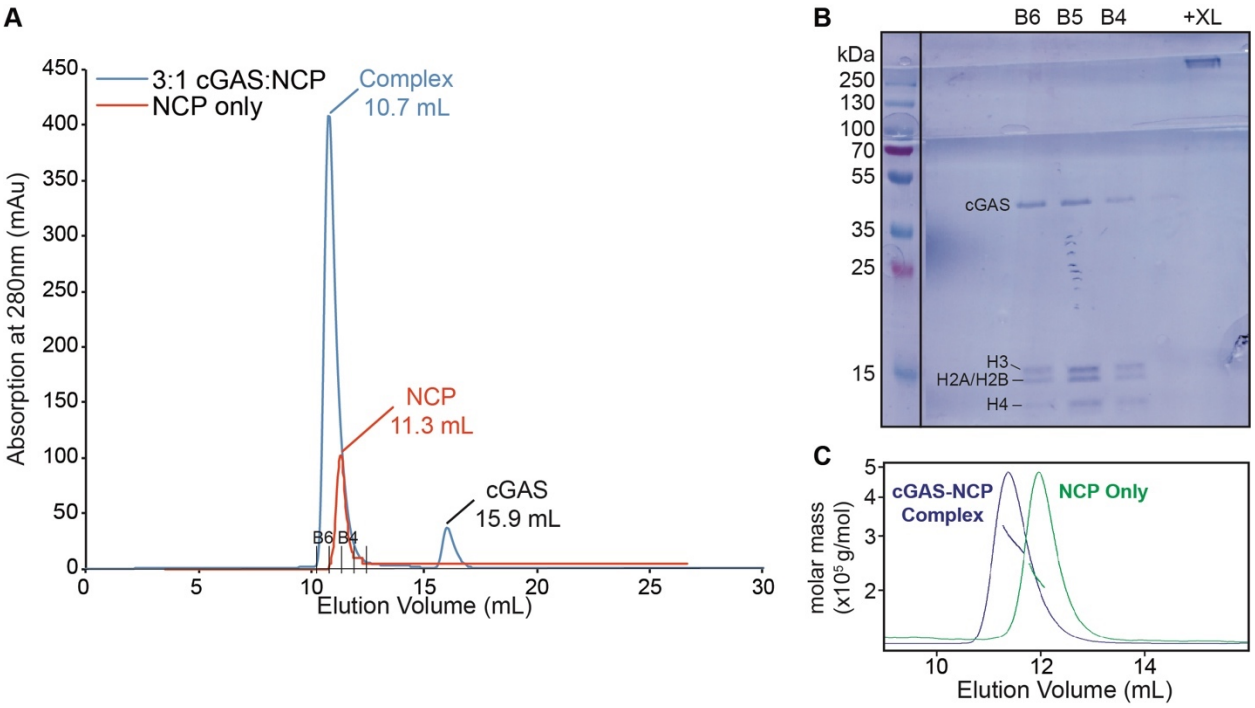

Fig. S1. cGAS: NCP complex purification. (**A**) Size-exclusion chromatogram of the nucleosome core particle (NCP) (red) and the assembled cGAS:NCP complex (blue) using a Superdex 200 increase 10/300GL gel filtration column and monitoring absorption at 280 nm. cGAS-NCP complex was loaded on preparative scale for cryo-EM sample preparation where both complex and residual unbound cGAS were observed. NCP only was loaded on analytical scale for retention time comparison. (**B**) SDS-PAGE analysis of the cGAS-NCP complex peak (lanes B6, B5, B4) and glutaraldehyde-crosslinked sample (lane +XL) to confirm complex size. (**C**) SEC-MALS analysis of the cGAS/NCP mixture at a molar ratio of 3:1 and free NCP using a Superdex 200 HR 10/300GL gel filtration column gave estimated molecular weights of 291.7 kDa for the cGAS-NCP complex and 209.4 kDa for free NCP, which are close to theoretical molecular weights of the 2:1 cGAS-NCP complex (291.3 kDa) and free NCP (205.5 kDa), respectively.

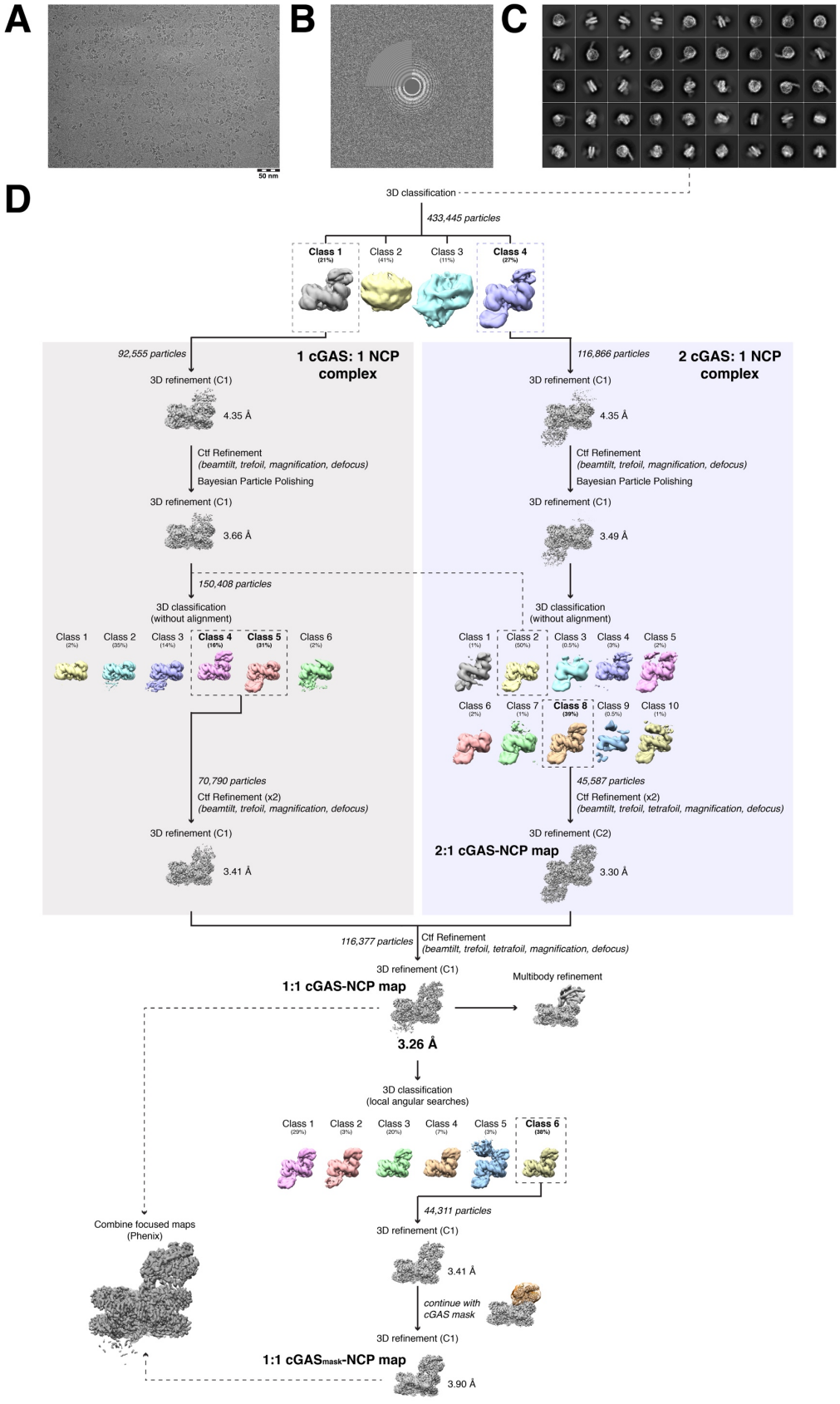
A
50 nm
B
C
D
3D classification
433,445 particles
Class 1 (21%)
Class 2 (41%)
Class 3 (11%)
Class 4 (27%)
92,555 particles
1 cGAS: 1 NCP complex
3D refinement (C1)
4.35 Å
Ctf Refinement
(beamtilt, trefoil, magnification, defocus)
Bayesian Particle Polishing
3D refinement (C1)
3.66 Å
150,408 particles
3D classification
(without alignment)
Class 1 (2%)
Class 2 (35%)
Class 3 (14%)
Class 4 (16%)
Class 5 (31%)
Class 6 (2%)
70,790 particles
Ctf Refinement (x2)
(beamtilt, trefoil, magnification, defocus)
3D refinement (C1)
3.41 Å
116,866 particles
2 cGAS: 1 NCP complex
3D refinement (C1)
4.35 Å
Ctf Refinement
(beamtilt, trefoil, magnification, defocus)
Bayesian Particle Polishing
3D refinement (C1)
3.49 Å
3D classification
(without alignment)
Class 1 (1%)
Class 2 (50%)
Class 3 (0.5%)
Class 4 (3%)
Class 5 (2%)
Class 6 (2%)
Class 7 (1%)
Class 8 (39%)
Class 9 (0.5%)
Class 10 (1%)
45,587 particles
Ctf Refinement (x2)
(beamtilt, trefoil, tetrafoil, magnification, defocus)
3D refinement (C2)
2:1 cGAS-NCP map
3.30 Å
116,377 particles
Ctf Refinement
(beamtilt, trefoil, tetrafoil, magnification, defocus)
3D refinement (C1)
1:1 cGAS-NCP map
Multibody refinement
3.26 Å
3D classification
(local angular searches)
Class 1 (29%)
Class 2 (3%)
Class 3 (20%)
Class 4 (7%)
Class 5 (3%)
Class 6 (38%)
44,311 particles
3D refinement (C1)
3.41 Å
continue with
cGAS mask
3D refinement (C1)
1:1 cGASmask-NCP map
3.90 Å
Combine focused maps
(Phenix)

Fig. S2. cGAS-NCP cryo-EM reconstruction. (**A**) Example cryo-EM image of cGAS-NCP complex, (**B**) CTF correction, and (**C**) reference-free 2D classifications. (**D**) Data analysis schematic showing refinement of 1:1 and 2:1 cGAS-NCP and 1:1 $cGAS_{mask}$-NCP reconstructed maps. A composite combined focused map was prepared using the 3.26 Å 1:1 cGAS-NCP and 3.9 Å 1:1 $cGAS_{mask}$-NCP maps.

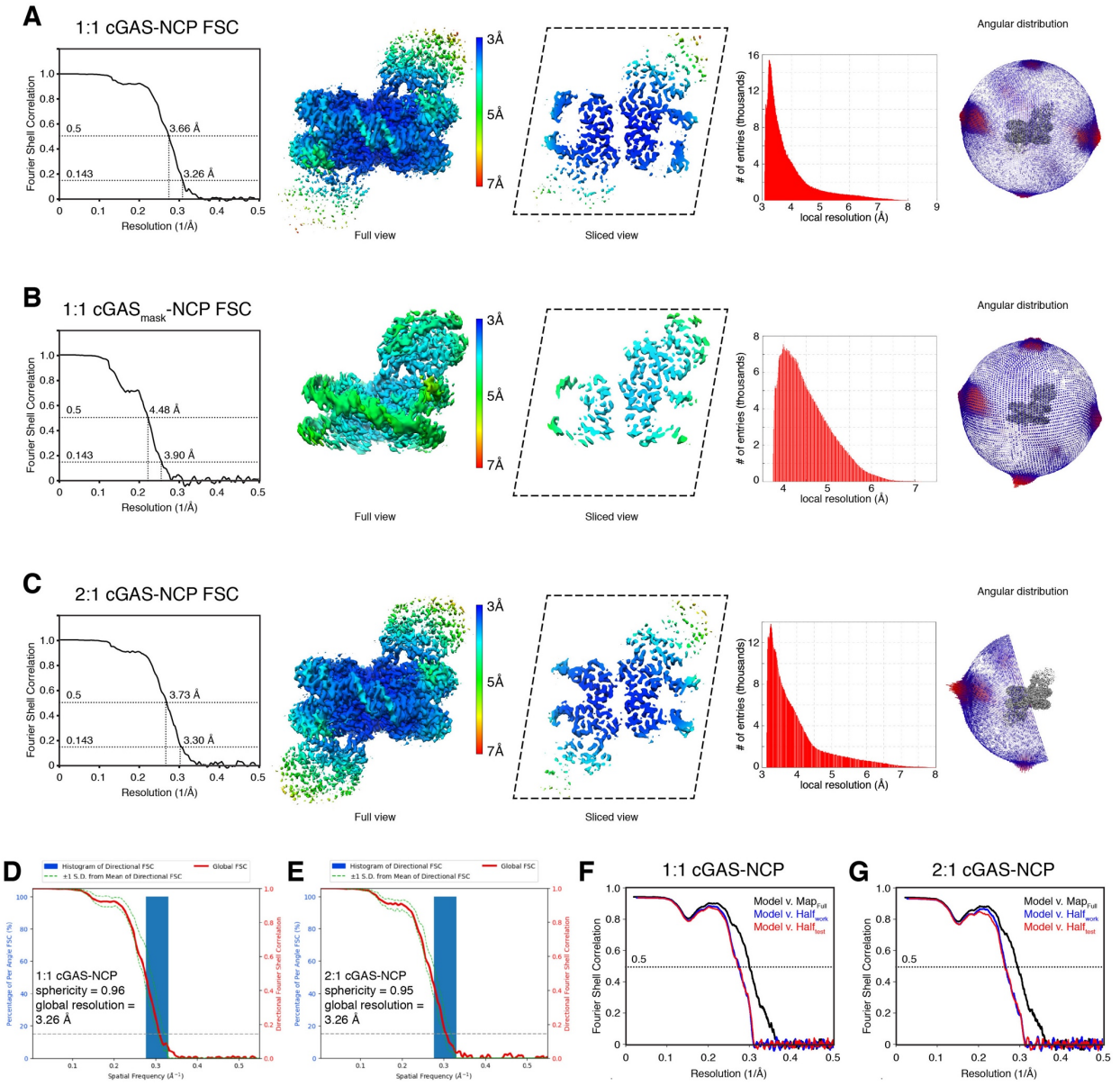

Fig. S3. Cryo-EM map and model validation. Fourier Shell Correlation (FSC) (left), local resolution displayed on full, masked map or map slice and histogram of local resolution (middle), and angular distribution of particles used for reconstruction (right) as assessed by Relion 3.1 for (**A**) 1:1 cGAS-NCP map (3.26 Å resolution), (**B**) 1:1 cGAS$_{mask}$-NCP map (3.9 Å resolution), and (**C**) 2:1 cGAS-NCP map (3.30 Å resolution). Resolution determined by the FSC 0.143 gold-standard method. (**D**) Histogram and directional FSC plot for 1:1 cGAS-NCP map generated with 3DFSC. (**E**) Histogram and directional FSC plot for 2:1 cGAS-NCP map generated with 3DFSC. (**F**) Map v. model FSC curves with 1:1 cGAS-NCP model and sharpened, masked full map (Map$_{Full}$, black), half-map used in final refinement (Half$_{work}$, blue) and half-map excluded from

final refinement ($Half_{test}$, red). (**G**) Identical map v. model FSC curves for 2:1 cGAS-NCP model. In both cases, half-maps correspond equally well to model suggesting lack of overfitting.

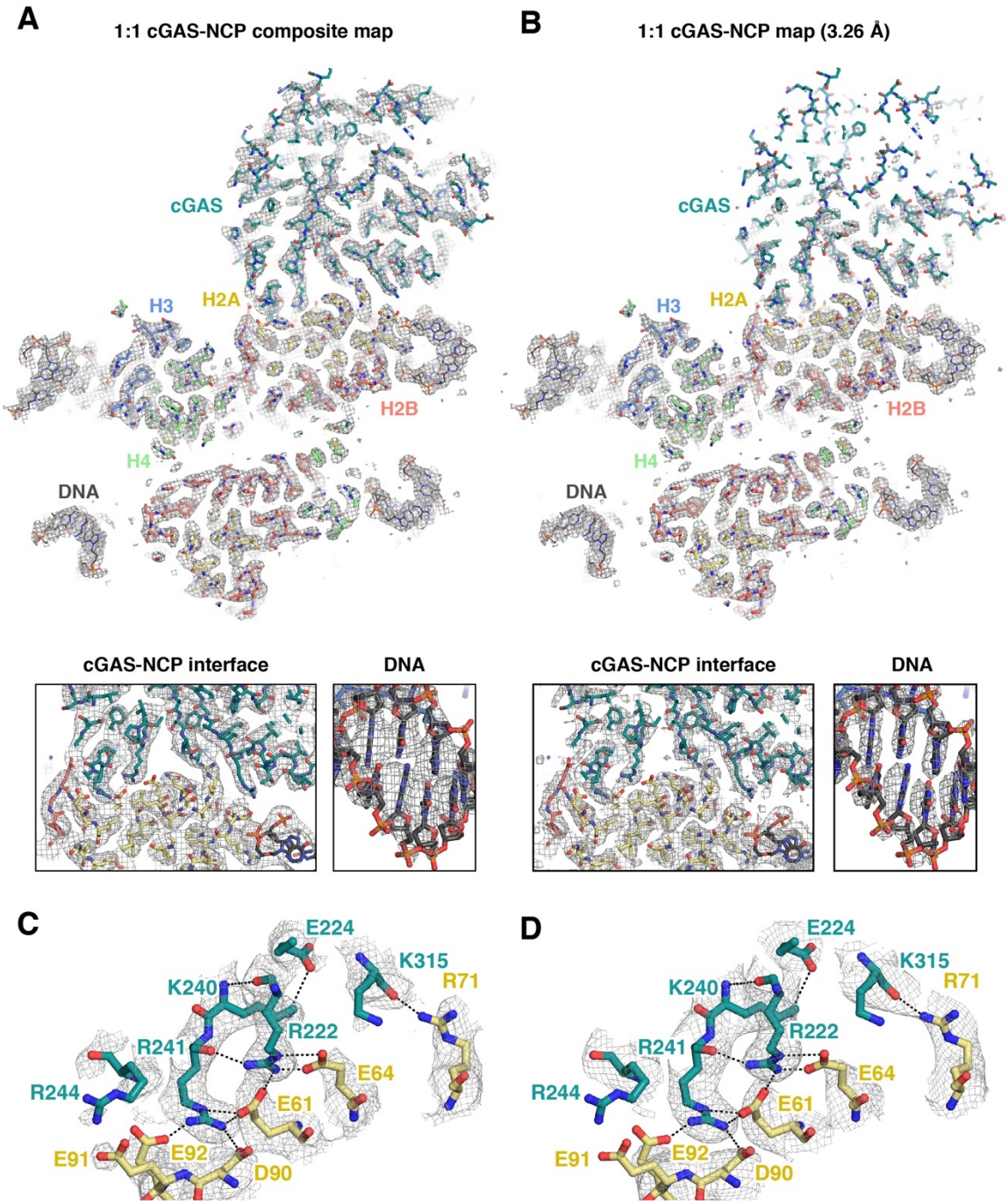

Fig. S4. Cryo-EM maps. (**A**) Slice view of 1:1 cGAS-NCP model with overlaid composite combined focused map with all components of model represented (top). Zoomed views of cGAS-NCP interface (bottom, left) and DNA (bottom, right). (**B**) Identical views of model with overlaid 3.26 Å 1:1 cGAS-NCP map. (**C**) Zoomed view of cGAS-NCP interface identical to Fig. 2B with composite combined focused map overlaid. (**D**) Identical view as in panel C with 3.26 Å 1:1 cGAS-NCP map overlaid.

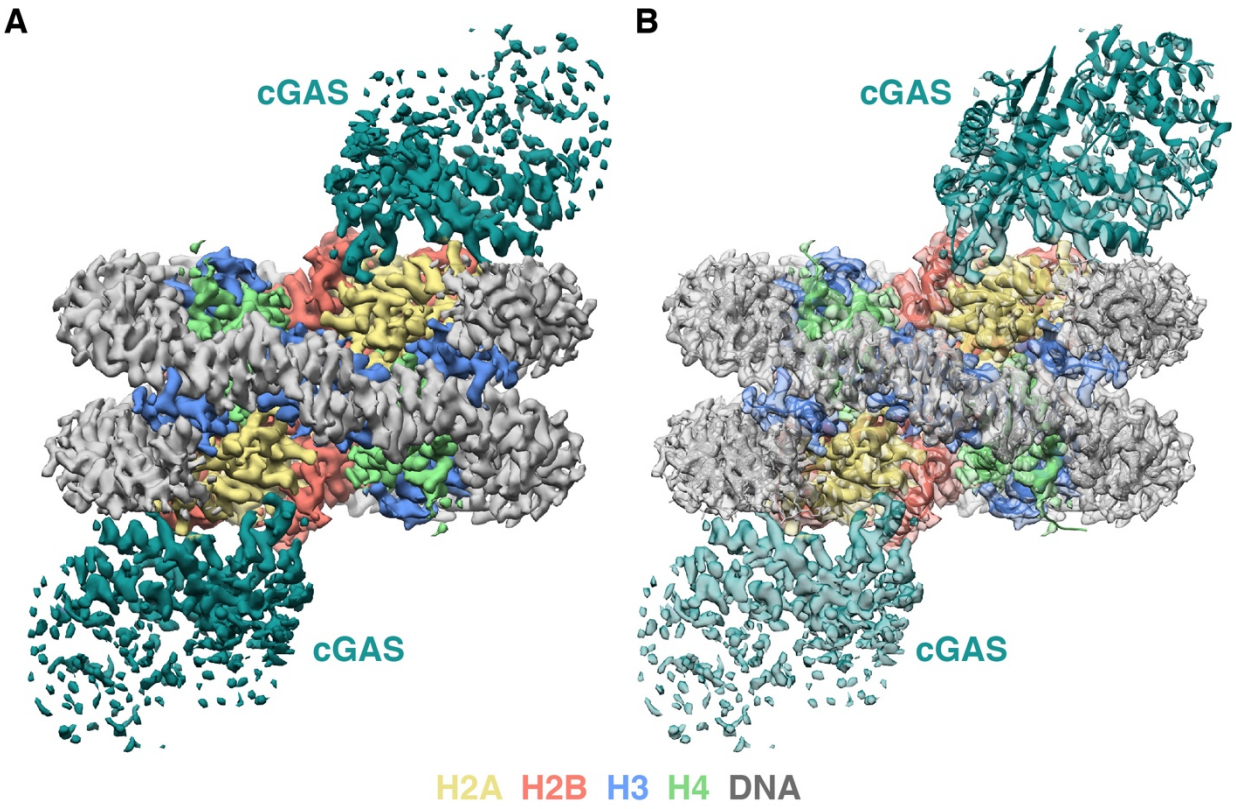

Fig. S5. Cryo-EM structure of 2:1 cGAS-NCP complex. (**A**) 3.30 Å resolution reconstructed map of the 2:1 cGAS-NCP complex, colored to correspond to model. (**B**) 2:1 cGAS-NCP model overlaid with transparent version of map in panel A. One cGAS chain is modeled into this map which was reconstructed with C2 symmetry.

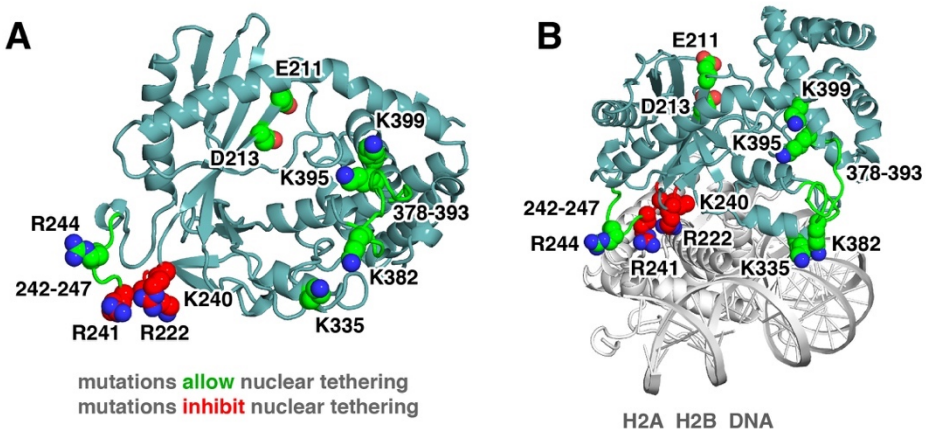

Fig. S6. Consequences of cGAS mutations on nuclear tethering. (**A**) cGAS from 1:1 cGAS-NCP model highlighting sites of previously reported mutations that inhibit (red) or allow (green) cGAS nuclear tethering. (**B**) Distinct view of mutants in panel A visualized on the H2A-H2B-DNA interface with the remainder of the NCP omitted for clarity.

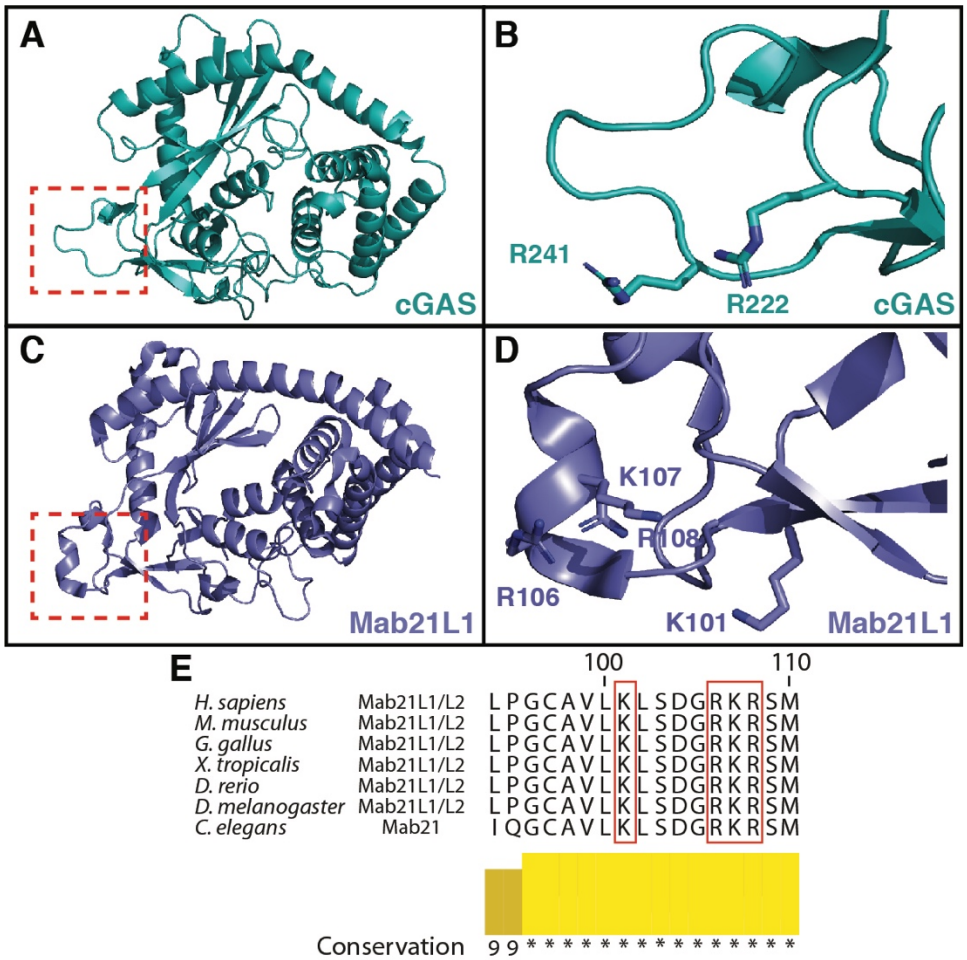

Fig. S7. Structural and sequence comparison between cGAS and Mab21L1/L2 proteins. (**A**) Structure of cGAS in the cGAS-NCP complex. Highlighted in the red dashed box is the loop region of cGAS that contains the conserved arginine anchors that bind to the nucleosome acidic patch. (**B**) Close-up view of the loop region highlighted in panel A. (**C**) Structure of human Mab21L1 (PDB: 5EOG chain H). Highlighted in red is the loop region of Mab21L1 that shares the same location to the arginine-anchor loop region of cGAS. (**D**) Close-up view of the loop region highlighted in panel C, where arginine and lysine residues are shown in sticks. (**E**) Multiple sequence alignment of the candidate Mab21-nucleosome-binding region based on structural alignment. Shown are numerical and histogram representations of the conservation score, where asterisks denote complete identity conservation (http://www.jalview.org/).

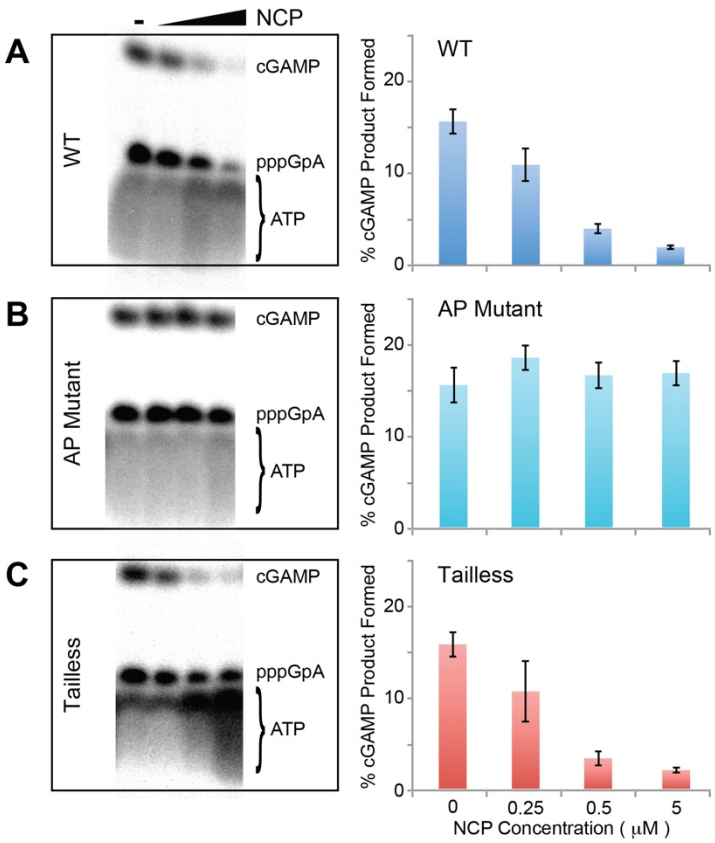

Fig. S8. Nucleosome core particle dependent cGAS activity assays. Representative TBE/7M Urea/15% PAGE gels and quantifications of cGAS (0.5 μM: 5 μM dsDNA) activity assays with (**A**) wild type, (**B**) acidic patch mutant (H2A E61A, E64S, N68A, D72S, N89A, D90A, E91S), and (**C**) tailless histone nucleosome core particles. Histograms are the average of three replicate measurements with standard deviation represented as error bars.

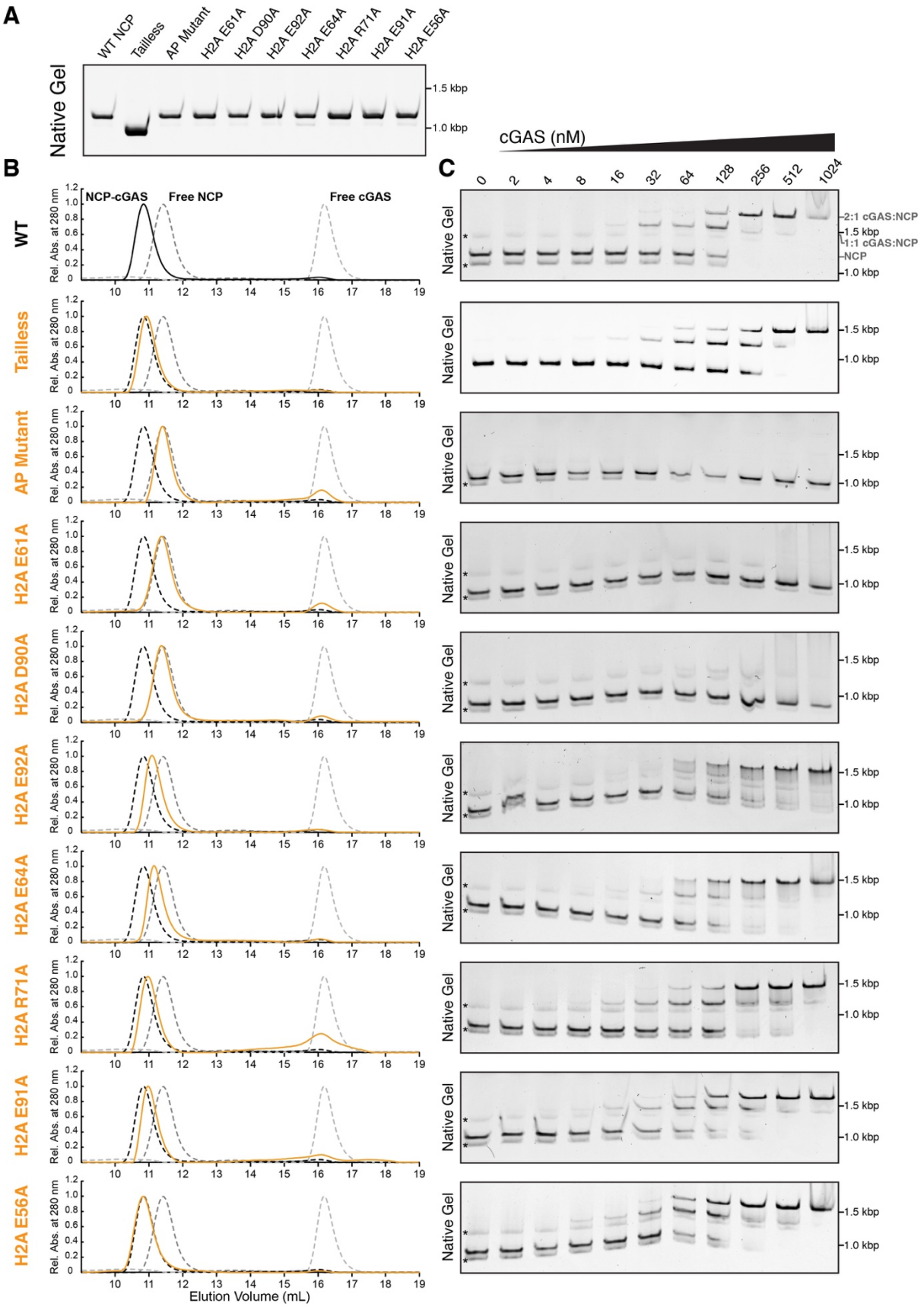
A
WT NCP
Tailless
AP Mutant
H2A E61A
H2A D90A
H2A E92A
H2A E64A
H2A R71A
H2A E91A
H2A E56A
Native Gel
1.5 kbp
1.0 kbp
B
C
cGAS (nM)
0
2
4
8
16
32
64
128
256
512
1024
NCP-cGAS
Free NCP
Free cGAS
WT
Tailless
AP Mutant
H2A E61A
H2A D90A
H2A E92A
H2A E64A
H2A R71A
H2A E91A
H2A E56A
Rel. Abs. at 280 nm
Native Gel
2:1 cGAS:NCP
1:1 cGAS:NCP
NCP
Elution Volume (mL)

Fig. S9. Characterizing binding between cGAS and NCP mutants by gel filtration and electrophoretic mobility shift assays. (**A**) Wild-type and mutant NCP (200 nM) separated on native 10% polyacrylamide gel, stained with ethidium bromide. (**B**) Size exclusion chromatograms of 3 μM : 1 μM mixture of cGAS and wild-type or mutant NCP using a Superdex 200 increase 10/300GL gel filtration column and monitoring absorption at 280 nm. Free wild-type NCP, free cGAS, and cGAS-NCP complex are shown for comparison. (**C**) Electrophoretic mobility shift assays (EMSA) with wild-type and mutant NCPs (25 nM) combined with varying concentrations of cGAS and separated on native 10% polyacrylamide gel, stained with ethidium bromide. Note: Minor instability is observed in NCP samples at the low concentration in EMSA conditions as indicated by asterisks. As shown in panel A, the overall integrity of NCP samples is strong as indicated by stability at the higher concentration of 200 nM, which is lower than concentrations used for structural and functional assays.

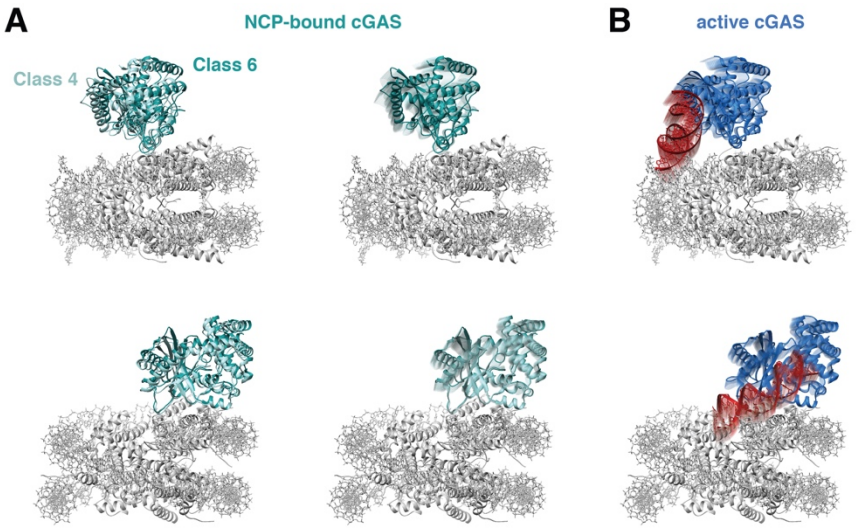

Fig. S10. Simultaneous binding of NCP and DNA at cGAS site A is permissible. (**A**) Two views of aligned docked models of cGAS-NCP complex in conformations observed for Classes 4 and 6 from Fig. 1D (left) and morphing between models (right). (**B**) Structure of active cGAS with site A DNA bound (PDBID: 4LEV) aligned to cGAS in morphed cGAS-NCP model in panel A.

Table S1. Cryo-EM data collection, refinement and validation statistics

	1:1 cGAS:NCP (EMDB-22408) (PDB 7JO9)	2:1 cGAS:NCP (EMDB-22409) (PDB 7JOA)	1:1 $cGAS_{mask}$:NCP (EMDB-22413)
Data collection and processing			
Magnification	57,500x	57,500x	57,500x
Voltage (kV)	200	200	200
Electron exposure (e–/Å^2)	53	53	53
Defocus range (μm)	-0.6 to -3.1	-0.6 to -3.1	-0.6 to -3.1
Pixel size (Å)	0.91	0.91	0.91
Symmetry imposed	C1	C2	C1
Initial particle images (no.)	737,361	737,361	737,361
Final particle images (no.)	116,377	45,587	44,311
Map resolution (Å)	3.26 (0.143)	3.30 (0.143)	3.90 (0.143)
FSC threshold			
Map resolution range (Å)	3.1-8.1	3.1-8.0	3.7-7.1
Refinement			
Initial model used (PDB code)	4LEV, 6FQ5	4LEV, 6FQ5	
Model resolution (Å)	3.3 (0.5)	3.4 (0.5)	
FSC threshold			
Map sharpening *B* factor (Å^2)	-86	-79	
Model composition			
Non-hydrogen atoms	14,994	14,994	
Protein residues	1,125	1,125	
Nucleotides	290	290	
Ligands	1	1	
B factors (Å^2)			
Protein	35.3	36.7	
Nucleotide	72.8	73.4	
Ligand	121.8	128.8	
R.m.s. deviations			
Bond lengths (Å)	0.008	0.009	
Bond angles (°)	0.730	0.772	
Validation			
MolProbity score	1.60	1.76	
Clashscore	4.77	6.07	
Poor rotamers (%)	0.41	0	
Ramachandran plot			
Favored (%)	94.9	93.5	
Allowed (%)	5.1	6.5	
Disallowed (%)	0	0	
Map-model correlation			
CC(mask)	0.82	0.82	
CC(box)	0.79	0.79	
CC(peaks)	0.73	0.72	
CC(volume)	0.80	0.80	
EMRinger Score	1.58	1.49	

Movie S1.
Overview of cGAS-NCP structure and mechanism of cGAS inhibition by NCP binding.

Movie S2.
Multibody analysis of cGAS-NCP conformational dynamics.

References and Notes:

1. R. Barbalat, S. E. Ewald, M. L. Mouchess, G. M. Barton, Nucleic acid recognition by the innate immune system. *Ann. Rev. Immunol.* **29**, 185-214 (2011).
2. J. Wu, Z. J. Chen, Innate immune sensing and signaling of cytosolic nucleic acids. *Ann. Rev. Immunol.* **32**, 461-488 (2014).
3. A. Ablasser, Z. J. Chen, cGAS in action: Expanding roles in immunity and inflammation. *Science* **363**, eaat8657 (2019).
4. L. Sun, J. Wu, F. Du, X. Chen, Z. J. Chen, Cyclic GMP-AMP synthase is a cytosolic DNA sensor that activates the type I interferon pathway. *Science* **339**, 786-791 (2013).
5. J. Wu *et al.*, Cyclic GMP-AMP is an endogenous second messenger in innate immune signaling by cytosolic DNA. *Science* **339**, 826-830 (2013).
6. H. Ishikawa, G. N. Barber, STING is an endoplasmic reticulum adaptor that facilitates innate immune signalling. *Nature* **455**, 674-678 (2008).
7. B. Zhong *et al.*, The adaptor protein MITA links virus-sensing receptors to IRF3 transcription factor activation. *Immunity* **29**, 538-550 (2008).
8. D. L. Burdette *et al.*, STING is a direct innate immune sensor of cyclic di-GMP. *Nature* **478**, 515-518 (2011).
9. H. E. Volkman, S. Cambier, E. E. Gray, D. B. Stetson, Tight nuclear tethering of cGAS is essential for preventing autoreactivity. *eLife* **8**, e47491 (2019).
10. H. Liu *et al.*, Nuclear cGAS suppresses DNA repair and promotes tumorigenesis. *Nature* **563**, 131-136 (2018).

11. M. Gentili *et al.*, The N-Terminal domain of cGAS determines preferential association with centromeric DNA and innate immune activation in the nucleus. *Cell Rep.* **26**, 2377-2393 (2019).

12. C. Zierhut *et al.*, The cytoplasmic DNA sensor cGAS promotes mitotic cell death. *Cell* **178**, 302-315 (2019).

13. H. Jiang *et al.*, Chromatin-bound cGAS is an inhibitor of DNA repair and hence accelerates genome destabilization and cell death. *EMBO J.* **38**, e102718 (2019).

14. M. Du, Z. J. Chen, DNA-induced liquid phase condensation of cGAS activates innate immune signaling. *Science* **361**, 704-709 (2018).

15. P. Gao *et al.*, Cyclic [G(2',5')pA(3',5')p] is the metazoan second messenger produced by DNA-activated cyclic GMP-AMP synthase. *Cell* **153**, 1094-1107 (2013).

16. F. Civril *et al.*, Structural mechanism of cytosolic DNA sensing by cGAS. *Nature* **498**, 332-337 (2013).

17. X. Li *et al.*, Cyclic GMP-AMP synthase is activated by double-stranded DNA-induced oligomerization. *Immunity* **39**, 1019-1031 (2013).

18. X. Zhang *et al.*, The cytosolic DNA sensor cGAS forms an oligomeric complex with DNA and undergoes switch-like conformational changes in the activation loop. *Cell Rep.* **6**, 421-430 (2014).

19. L. Andreeva *et al.*, cGAS senses long and HMGB/TFAM-bound U-turn DNA by forming protein-DNA ladders. *Nature* **549**, 394-398 (2017).

20. W. Zhou *et al.*, Structure of the human cGAS-DNA complex reveals enhanced control of immune surveillance. *Cell* **174**, 300-311 (2018).

21. W. Xie *et al.*, Human cGAS catalytic domain has an additional DNA-binding interface that enhances enzymatic activity and liquid-phase condensation. *Proc. Natl. Acad. Sci. USA* **116**, 11946-11955 (2019).

22. S. Bilokapic, M. Strauss, M. Halic, Structural rearrangements of the histone octamer translocate DNA. *Nat. Commun.* **9**, 1330 (2018).

23. X. Wu *et al.*, Molecular evolutionary and structural analysis of the cytosolic DNA sensor cGAS and STING. *Nucleic Acids Res.* **42**, 8243-8257 (2014).

24. D. C. Hancks, M. K. Hartley, C. Hagan, N. L. Clark, N. C. Elde, Overlapping patterns of rapid evolution in the nucleic acid sensors cGAS and OAS1 suggest a common mechanism of pathogen antagonism and escape. *PLoS Genet.* **11**, e1005203 (2015).

25. M. Mariani *et al.*, Two murine and human homologs of mab-21, a cell fate determination gene involved in Caenorhabditis elegans neural development. *Hum. Mol. Genet.* **8**, 2397-2406 (1999).

26. C. C. de Oliveira Mann, R. Kiefersauer, G. Witte, K. P. Hopfner, Structural and biochemical characterization of the cell fate determining nucleotidyltransferase fold protein MAB21L1. *Sci. Rep.* **6**, 27498 (2016).

27. B. Fierz, M. G. Poirier, Biophysics of chromatin dynamics. *Ann. Rev. Biophys.* **48**, 321-345 (2019).

28. A. A. Kalashnikova, M. E. Porter-Goff, U. M. Muthurajan, K. Luger, J. C. Hansen, The role of the nucleosome acidic patch in modulating higher order chromatin structure. *J. R. Soc., Interface* **10**, 20121022 (2013).

29. R. K. McGinty, S. Tan, Recognition of the nucleosome by chromatin factors and enzymes. *Curr. Opin. Struct. Biol.* **37**, 54-61 (2016).

30. R. D. Makde, J. R. England, H. P. Yennawar, S. Tan, Structure of RCC1 chromatin factor bound to the nucleosome core particle. *Nature* **467**, 562-566 (2010).

31. K. J. Armache, J. D. Garlick, D. Canzio, G. J. Narlikar, R. E. Kingston, Structural basis of silencing: Sir3 BAH domain in complex with a nucleosome at 3.0 A resolution. *Science* **334**, 977-982 (2011).

32. R. K. McGinty, R. C. Henrici, S. Tan, Crystal structure of the PRC1 ubiquitylation module bound to the nucleosome. *Nature* **514**, 591-596 (2014).

33. C. J. Anderson *et al.*, Structural basis for recognition of ubiquitylated nucleosome by Dot1L methyltransferase. *Cell Rep.* **26**, 1681-1690 (2019).

34. A. Skrajna *et al.*, Comprehensive nucleosome interactome screen establishes fundamental principles of nucleosome binding. *Nucleic Acids Res.* (2020). doi: 10.1093/nar/gkaa544.

35. R. M. Glaeser, D. Typke, P. C. Tiemeijer, J. Pulokas, A. Cheng, Precise beam-tilt alignment and collimation are required to minimize the phase error associated with coma in high-resolution cryo-EM. *J. Struct. Biol.* **174**, 1-10 (2011).

36. M. A. Herzik, Jr., M. Wu, G. C. Lander, High-resolution structure determination of sub-100 kDa complexes using conventional cryo-EM. *Nat. Commun.* **10**, 1032 (2019).

37. D. N. Mastronarde, Automated electron microscope tomography using robust prediction of specimen movements. *J. Struct. Biol.* **152**, 36-51 (2005).

38. J. Zivanov, T. Nakane, S. H. W. Scheres, Estimation of high-order aberrations and anisotropic magnification from cryo-EM data sets in RELION-3.1. *IUCrJ* **7**, 253-267 (2020).

39. A. Rohou, N. Grigorieff, CTFFIND4: Fast and accurate defocus estimation from electron micrographs. *J. Struct. Biol.* **192**, 216-221 (2015).

40. Y. Z. Tan *et al.*, Addressing preferred specimen orientation in single-particle cryo-EM through tilting. *Nat. Methods* **14**, 793-796 (2017).

41. P. V. Afonine *et al.*, Real-space refinement in PHENIX for cryo-EM and crystallography. *Acta Crystallogr. D, Struct. Biol.* **74**, 531-544 (2018).

42. V. B. Chen *et al.*, MolProbity: all-atom structure validation for macromolecular crystallography. *Acta Crystallogr. D, Biol. Crystallogr.* **66**, 12-21 (2010).

43. B. A. Barad *et al.*, EMRinger: side chain-directed model and map validation for 3D cryo-electron microscopy. *Nat. Methods* **12**, 943-946 (2015).

44. M. L. Dechassa *et al.*, Structure and Scm3-mediated assembly of budding yeast centromeric nucleosomes. *Nat. Commun.* **2**, 313 (2011).